Experimental study of neutron-rich Li isotopes

Progress report

Jesper Halkjær Jensen

Supervisor: Karsten Riisager

July 26, 2017

CERN-THESIS-2017-454
//2017

1 Introduction

The field of nuclear physics saw the light of day when Rutherford discovered the atomic nucleus in 1911[1]. He bombarded a gold foil with α-particles and saw that some of the atoms were reflected in backward angles. To explain this he theorized a compact core containing most of the mass and all the positive charge of the nucleus.

Today we know that the size of the atomic nucleus is at least four orders of magnitudes smaller than the atom itself. We also know that the core consists of positively charged protons and neutral neutrons, collectively called nucleons. They are held together by the strong nuclear force, described by QCD.

We can compose many different isotopes by combinations of nucleons and protons to make up the whole nuclear chart. Many of these isotopes have been studied extensively, but some are easier than others. Nature favors a roughly equal amount of protons and neutrons, a region in the nuclear chart called the "valley of stability". As we move away from this area, the nuclei start to become unstable and decay. In the most extreme cases where the last proton or neutron is just barely bound we say we have reached the *drip lines*. The lifetime of these extreme systems are typically very small, making it an experimental challenge to study them.

It is, however, also at the drip lines where we see interesting systems such as halo nuclei. That is nuclei, where the spatial distribution is much larger than the natural length scale or, to put it in other words, a system where some subsystem spends most of it's time outside the classical allowed region [2]. An example is ^{11}Li, which is almost a big as a lead nucleus, even though lead have $\sim$200 nucleons and ^{11}Li only have 11 [3].

We can in principle describe the structure of a nucleus with the full wavefunction, computed from QCD, but it is typically far to complex to construct. Instead other models based on different assumptions have been developed.

In one extreme we have the *liquid drop model*, which treat the nucleus as a uniform sphere of nuclear matter. The structure and features described by this model are analogous to a droplet of liquid. A great success of this model was the development of the Semi-Emperical Mass Formula, which describes the trend in binding energies very well across the nuclear chart.

In the other end we have independent particle models, which treats each nucleon as moving in an effective potential mediated by the rest of the nucleus. In this regime, the shell model has been a great success. It is analogous to the description of the electronic wavefunctions in the Coulomb field. Due to the complicated nature of the strong force and many-particle dynamics,

however, a phenomenological potential must be used. One of the main achievements of this model is the reproduction of the so called *magic numbers*, which is certain numbers of neutrons or protons that are particularly strong bound.

The true nuclear structure, of course, lies somewhere in between the liquid drop model and the independent particle model, but these model are nonetheless extremely useful.

In my PhD I will be looking a neutron rich Lithium isotopes, which are best described in the shell model picture. The main objective is an experimental investigation of ^{11}Li via neutron transfer, but also ^{10}Li and ^{9}Li are important pieces to understand ^{11}Li. The experiment to study ^{11}Li has already been granted beam time at the ISOLDE facility at CERN, but has not been fully carried out yet.

I started my PhD with data from an experiment carried out in 2005. I will refer to this experiment as IS367. It was also performed at ISOLDE. In this experiment a ^{9}Li beam was incident on a deuterated target at 2.3 MeV/A. The goal was to study ^{10}Li and subsequently also ^{9}Li and ^{8}Li via neutron transfer. Both ^{9}Li and ^{10}Li are important pieces in the ^{11}Li puzzle. This reaction is very similar to the reaction we will use for the ^{11}Li experiment, but with tritons instead of deuterons. This will let us reach ^{11}Li with two-neutron transfer.

During 2016 a new post-accelerating unit was installed at ISOLDE, making it possible to reach beam energies up 7MeV/A. This is the energy region we wanted to perform the experiment to study ^{11}Li. However, for this experiment we have designed an entirely new setup. In an combined effort to commission the new setup, and contribute with more experimental data on ^{10}Li in this energy region, we carried out another ^{9}Li on deuterons experiment in the fall of 2016. I will refer to this experiment as IS561.

Since the Summer of 2016 I have been preparing for this experiment and afterwards analyzing the data. Understanding the strengths and weaknesses of the setup is important for the success of the more difficult triton target, which will be carried out in the fall of 2017.

2 The physics cases of ^{10}Li, ^{11}Li and ^{8}Li

The interpretation of ^{11}Li as a halo nucleus goes back to 1985, when Tanihata et al. [3] discovered a sudden increase in the mass radius of ^{11}Li, see Figure 2.1a. The two-neutron separation energy has since been measured to $369(15)$ keV[4]. The low binding energy and the large matter radius, suggests that the two neutrons are mostly located outside the classically allowed regions. This is exactly the behavior we classify as a halo nucleus [2]. In this case we think of ^{11}Li as made up by a ^{9}Li core with two neutrons orbiting it. Such a structure seems fit for a single particle description via the shell model, or even an interacting three-body model.

The exotic structure of ^{11}Li, breaks the predicted $N = 8$ magic number. This has been known for a long time [5]. The current consensus is that the ground state is a roughly equal mixture of a $2s_{1/2}$ and a $1p_{1/2}$ state for the valence neutrons. In Figure 2.1b, we see a sketch of the shell model. On the left is the simple shell model predictions. On the right is a the evolution as seen in ^{11}Li, ^{10}Li and their neighbors. The $1p_{1/2}$ state is usually lower than the $2s_{1/2}$ state, but for the $N = 7, 8$ isotones, these levels are inverted. That means the $2s_{1/2}$ state fills the gap between the $1p_{1/2}$ and the $1d_{5/2}$, removing the $N = 8$ as a magic number, but introducing $N = 16$. The behavior of the $2s_{1/2}$ state is therefore important to understand the formation of halo nuclei [6].

The spin and parity of the ground state is agreed to be $3/2^-$ state, just like ^{9}Li. Despite the inversion of the neutron states, it is the last proton that dictates the spin and parity of the ground state. However, going up in excitation energy, there are little consensus on spin and parity of the excitated states of ^{11}Li [4]. The decay model of ^{11}Li, is also still debated. A recent study claims that it can not be a sequential decay [8], however, earlier experiments suggest both

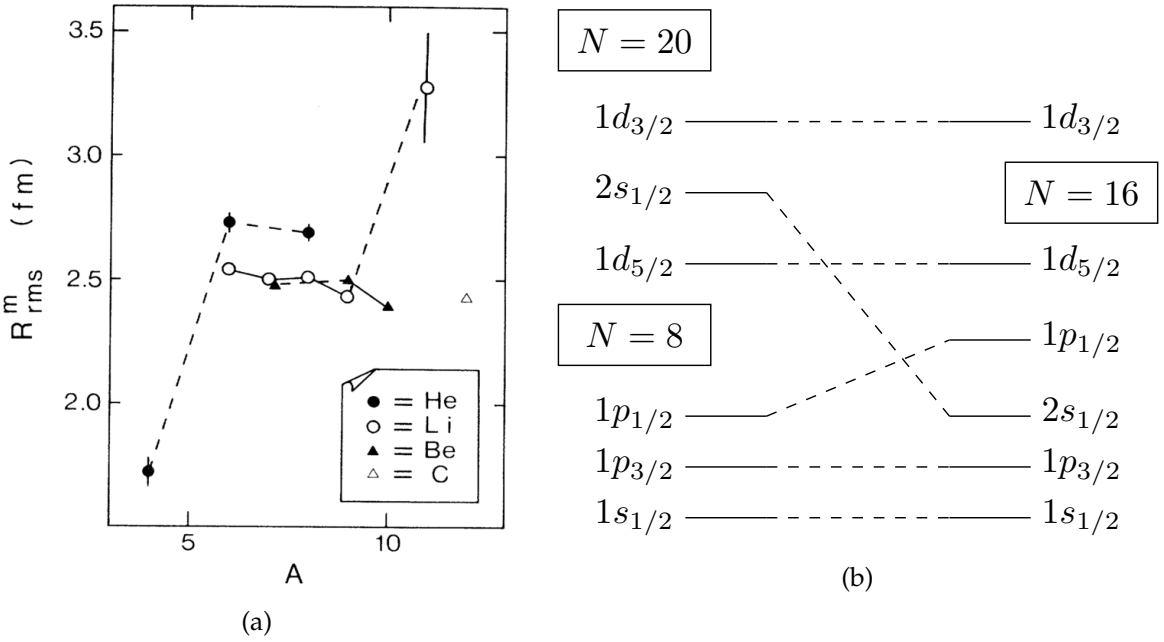

Figure 2.1: **(a)** Measurement of the mass radius for different Li, Be, He, C isotopes. A sudden increase in the masse of ^{11}Li suggests a two-neutron halo interpretation of the nucleus. Tanihata et al. [3] **(b)** Sketch of the inversion of the $2s_{1/2}$ and $1p_{1/2}$ states. The left side shows the simple shell model [7] and the right side shows the inversion as seen in N=7 and N=8 isotones.

sequential [9], phase-space [10] and dineutron[11] decays. To get a deeper understanding of ^{11}Li, however, we need more experimental data on the excited states in particular.

The theoretical understanding of ^{11}Li relies heavily on the unbound ^{10}Li nucleus, one of the $N = 7$ isotones. Since ^{10}Li is unbound, we refer to ^{11}Li as a Borremean system. The removal of a single neutron makes it unstable against neutron emission, just like the Borremean rings fall apart if you remove any single ring. The theoretical dependence on a good understanding of the ^{10}Li system have resulted in many experimental approaches[12]. Nonetheless, the ground state of ^{10}Li still under much debate.

The simplest shell model prediction is a $1p_{3/2}$ proton that couples to either a $1p_{1/2}$ or $1p_{3/2}$ and give either a 1^+ or 2^+. Due to the shell inversion of the $2s_{1/2}$ state we also consider a s-wave coupling. The current consensus is either a s-resonance or p-resonance coupling to the ^{9}Li ground state $3/2^-$. There are, however, theoretical predictions of both being the lowest energy state[13, 14].

The neutron s-wave is, however, considered a virtual state. The existence of such a virtual state was shown to be crucial to understanding the observed ^{10}Li fragmentation from an ^{11}Li experiment [13].

A p-wave resonance have been observed at several different experiments, typically located around 0.5 MeV above the ^{9}Li + n threshold. In an experiment similar to mine[15], they for instance observed a 0.38 MeV resonance. A recent experiment observed a $p_{1/2}$ state at 0.45 MeV but no evidence of an s-wave contribution [16].

It is important to note, that no matter what the ground state spin turns out to be in ^{10}Li, this may not be directly translatable to the coupling of the last neutron in ^{11}Li. The coupling of the last neutron can easily mix the states of the ^{10}Li system.

To unravel these mysteries, more experimental data on both the ^{10}Li and ^{11}Li systems is needed to guide the theoretical models, especially in the excited spectra. The understanding of ^{10}Li must be reliable such that we can use it in theoretical descriptions of ^{11}Li.

Due to the experimental method, described in the next section, we will also investigate ^{8}Li. From a nucelar structure point of view, ^{8}Li presents a puzzle, namely a missing 0^+ state. Both the proton and neutron in ^{8}Li is situated in a $p_{3/2}$ state, and can thus couple to both 0^+, 1^+, 2^+ and 3^+. This is also the predictions of both shell-model calculations[17, 18] and *ab initio* calculations [19–21]. The last three states have been observed at 0.98 MeV, g.s. and 2.26 MeV respectively. However, the 0^+ state has yet to be observed. It is expected to be around 2 MeV-4 MeV, but it may be hidden in the 3^+ state which is fed strongly.

3 Experimental approach

We investigate ^{11}Li and ^{10}Li with a nuclear reaction probe. Starting with ^{9}Li we reach the target isotopes by neutron transfer reactions. By bombarding ^{9}Li with either deuterons or tritons, we can transfer one or two neutrons to ^{9}Li and reach the isotopes of interest. Due to the short life time of ^{9}Li, 178.3(4) ms [12], however, it is not feasible to use ^{9}Li as a target. Instead we take advantage of the great advances in the technique of **R**adioactive **I**on **B**eams (RIB) and use ^{9}Li as the beam. The ISOLDE facility at CERN provides, among other facilities around the world, radioactive beams of ^{9}Li. With the newest upgrade to the post-acceleration unit of ISOLDE, HIE-ISOLDE, we can currently reach beam energies up to 7MeV/A.

With the beam being the heavier particle in the reaction we enter the regime of inverse kinematics where the center of mass follows the beam particle, making the kinematics in center of mass quite different from the laboratory frame. This changes not only the angle of the particles but also the solid angles, and this is very important in the calculation of differential cross sections.

To detect the charged reaction product we use segmented silicon strip detectors. These detectors gives us information about both energy and position. We can thus measure both the excitation spectrum and the angular distributions.

The nucleon transfer approach is excellent to probe single particle states. The structure of such states is described by a core nucleus and the nucleon in question. Single nucleon transfer reactions preferentially populate these states, suppressing the more complicated mixing of the single particle states [22].

The energy range provided by ISOLDE is optimal in the sense, that we want the reactions to be rather peripheral. If the beam energy is to low, we just see the Coulomb interaction. If the energy is too high, we will induce deep reactions, and we can not map out the single particle states.

Another reason for starting with ^{9}Li is to populate the states in ^{11}Li directly, and not via the ground state in ^{11}Li. A recent study [23] identified a structure at 1.03(3) MeV. Several other experiments have seen a structure around 1.3 MeV[24, 25]. However, this has been questioned from a theoretical point of view [26] and calculations suggest is a dipole resonance from the reaction mechanism [27]. By populating from ^{9}Li we can shed light on this possible resonance. Situations such as this one, makes it very important to study these system from many different starting points and with different reaction mechanisms.

3.1 ISOLDE

The radioactive beams of ^{9}Li for the experiments was (and will be) produced at ISOLDE, CERN [28]. It uses the **I**sotope **S**eperation **O**n-**L**ine-method[REF] to create and transport isotopes of interest to an experiment site. An overview of the complex is shown in Figure 3.1. The CERN accelerator complex delivers 1.4 GeV protons to ISOLDE which hits a heavy target, such as UC_x. This induces spallation, fragmentation and fission which in turn produce a wide array of different light nuclei. The light fragments diffuse into an ion source, where they are laser ionized and transported to a mass seperator which isolates the isotope of interest. ISOLDE provides two seperators, the **H**igh **R**esolution **S**eperator (HRS) and the **G**eneral **P**urpose **S**eperator(GPS). The resulting beam at 60 keV is delivered at the experiment.

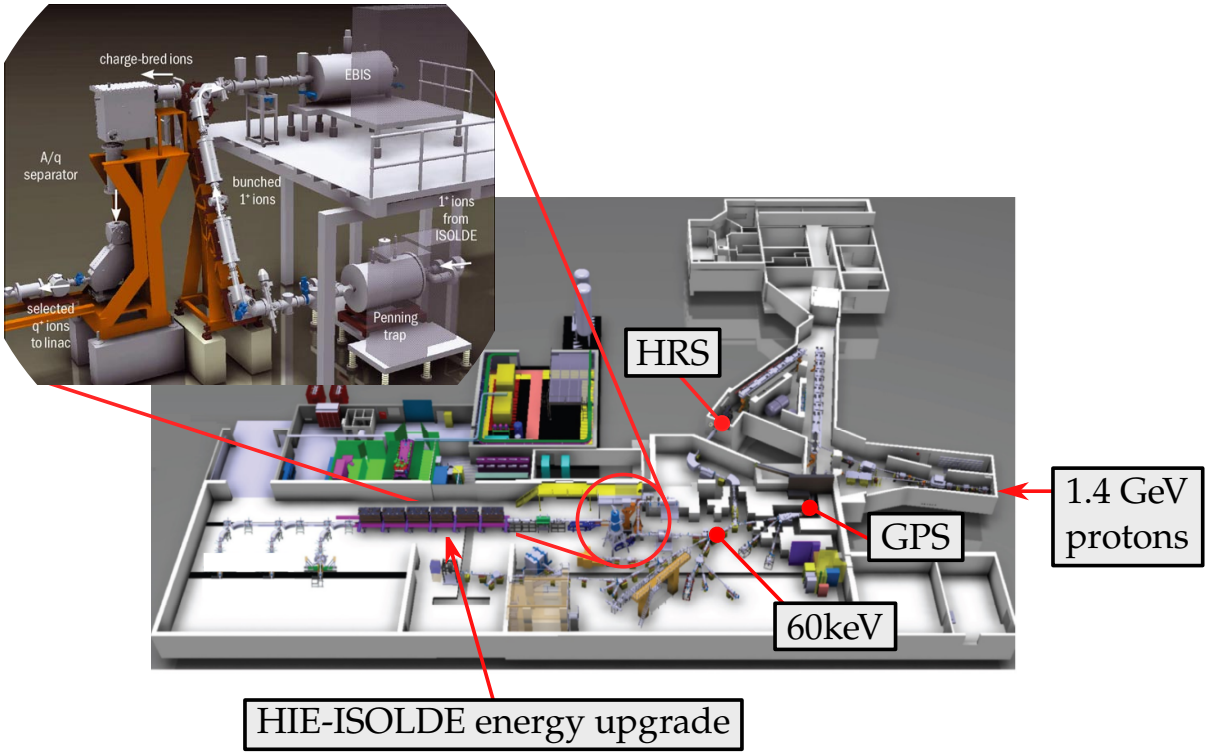

Figure 3.1: Overview of the ISOLDE facility. Images taken from [28].

HIE-ISOLDE

For reaction experiments, however, 60 keV are not sufficient. Therefore a post-accelerator, REX-ISOLDE, was installed between 2001 and 2005, reaching beam energies of up to 3 MeV/A. The idea is to ionize them even to higher charge states and accelerate them through a linear accelerator. The acceleration step was further upgraded as a part of the HIE-ISOLDE upgrade and reached beam energies of 7 MeV/A.

The post acceleration principle is shown in the inset in Figure 3.1. The ions from the ISOLDE beam are trapped, cooled and bunched in a Penning trap. They are then sent into an **E**lectron **B**eam **I**on **S**ource (EBIS), which creates highly charged ions. Before these highly charged ions are sent into a linear accelerator, they need to be mass separated once again. This is due to the buffer gasses used to cool the ISOLDE beam in the Penning trap.

Before the HIE-ISOLDE upgrade, the linear accelerator could reach 3 MeV/A. During the last decade a number of superconducting modules were designed and installed in order to reach even higher energies. In 2016 three of the 5 planned modules were installed. This enabled us to reach 6.72 MeV/A for the experiment during the fall.

3.2 Detection system

The two experiments have different setups, but some of the principles are common and will be explained in this section. The details on the specific setups will be discussed in later sections.

Detectors

We use silicon detectors to detect the charged particles. We mainly use two types, double-sided stip detectors (DSSD) and single-sided unsegmented detectors (pad). The pad detectors are a single piece of silicon. They are typically approximately 5cm by 5cm, and does therefore not provide positional information.

For the DSSDs, each side is subdivided into a number of strips, arranged in a grid. The strips of each side are orthogonal, effectively creating a number of pixels, analogous to a camera chip. When a charged particle enters the detector, it gradually loses energy by creation of electron-hole pairs. Due to an applied bias voltage the pairs will drift to the surface, where they are collected on metal contacts, and we read out this signal. Matching the two strips, we get the position where the particle hit the detector. We can calculate the position in space of the measured particle, if we know the where the detector is located. If we also know the beam properties, we can calculate the direction and thus the momentum of the measured particle.

In the experiments we use three types of DSSD's:

- **W1:** Square detector with 16x16 strips.
- **BB7:** Square detector with 32x32 strips.
- **S3:** Round detector with 32 spokes and 24 rings.

which can schematically be seen in Figure 3.2.

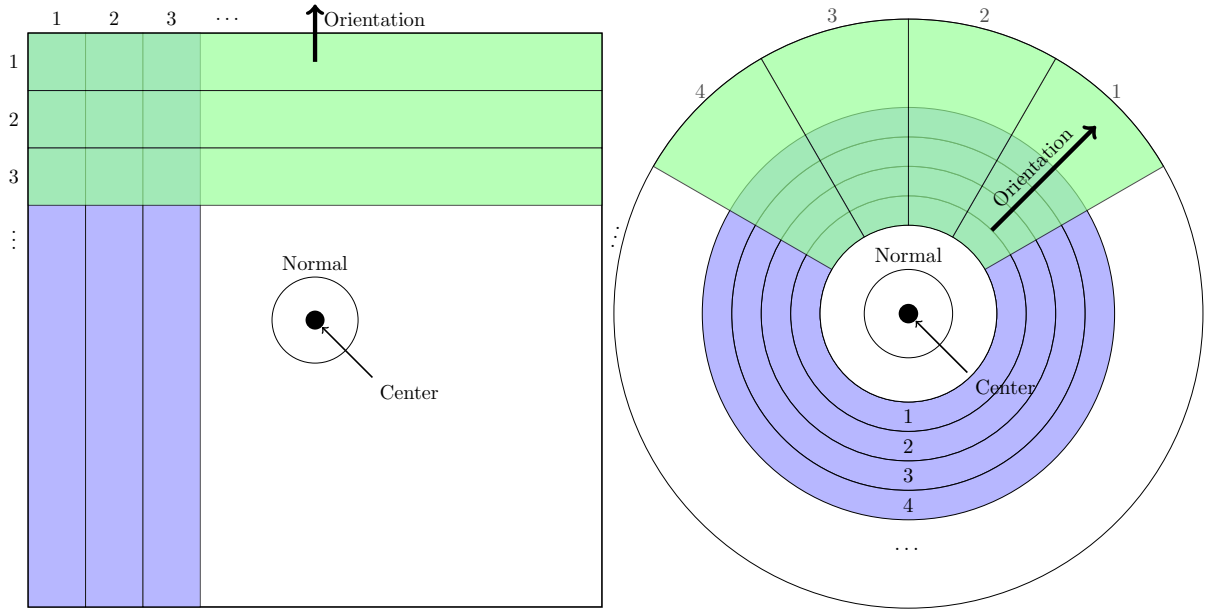

Figure 3.2: *Schematic overview of the detector types. Both the **W1** and **BB7** are of the rectangular shape, and the **S3** is the round. With courtesy of Michael Munch.*

3.3 Particle identification

To distinguish between different particles, we place a thin DSSD in front of a thicker pad. Typically the DSSD is around 60 µm whereas the pad is 1 mm-1.5 mm. We call this configuration a *telescope*. We will refer to the DSSD as the *front detector* and the pad as the *back detector*.

Different particles will deposit a fraction of their energy in the front detector and will be stopped in the back detector. The correlation between the deposited energy in the front detector and back detector is unique for different particle types. If we plot the deposited energy in the front detector, ΔE versus the deposited energy in the back detector, E, we can distinguish different particle types. See Figure 3.4 (a).

The deposited energy in the front detector depends on the effective thickness the particle have penetrated, which in turns depend on the incident angle

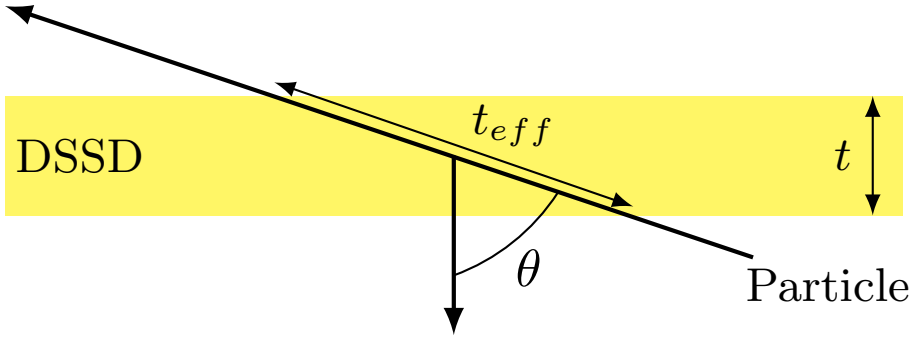

Figure 3.3: The angle, θ, between the normal of the detector and the particle determines the actual length t_{eff} the particles travel in the detector.

$$t_{eff} = \frac{t}{\cos(\theta)}, \tag{3.1}$$

where t is the nominal thickness of the detector and θ is the angle between the normal of the detector and the incoming particle, see Figure 3.3.

With many particles coming from many different angles, the deposited energy varies quite a lot, widening the bands we see in the $dE - E$ plot. It is hard to distinguish between the three particles in the lower region in Figure 3.4. If we correct for this effect, however, we can increase the resolution in the $dE - E$ plot quite significantly.

If we assume the energy loss is approximately constant through the front detector, the energy lost in the front detector will be proportional to the thickness,

$$dE = \frac{dE}{dx} \cdot t. \tag{3.2}$$

For a particle incident at some angle, θ, this translate to a larger energy loss

$$dE = \frac{dE}{dx} \cdot t_{eff} = \frac{dE}{dx} \cdot \frac{t}{\cos(\theta)} = \frac{dE'}{\cos(\theta)}, \tag{3.3}$$

where dE' is the corresponding energy loss if the particle had entered the front detector orthogonally, and is thus independent of the direction. With this correction, we get a much tighter $dE - E$ spectrum.

The remaining energy is deposited in the back detector, and the total correction is

$$\begin{aligned} dE' &= dE \cdot \cos(\theta) \\ E' &= E + dE \cdot (1 - \cos(\theta)), \end{aligned} \tag{3.4}$$

where E is the measured energy in the back detector and dE is the energy measured in the front detector and θ is the angle between the particle and the normal of the detector. In Figure 3.4(b) we see an example of an with this correction. Notice how the three particles in the lower regions are much better resolved.

3.4 Energy Calibration

To calibrate the detectors, we use an α-source with a well known spectrum. The α-source is placed at a known position, usually at the target position, and for each strip in the DSSD we get a spectrum given in raw channels. We fit Gaussians to the peaks to get the channel corresponding

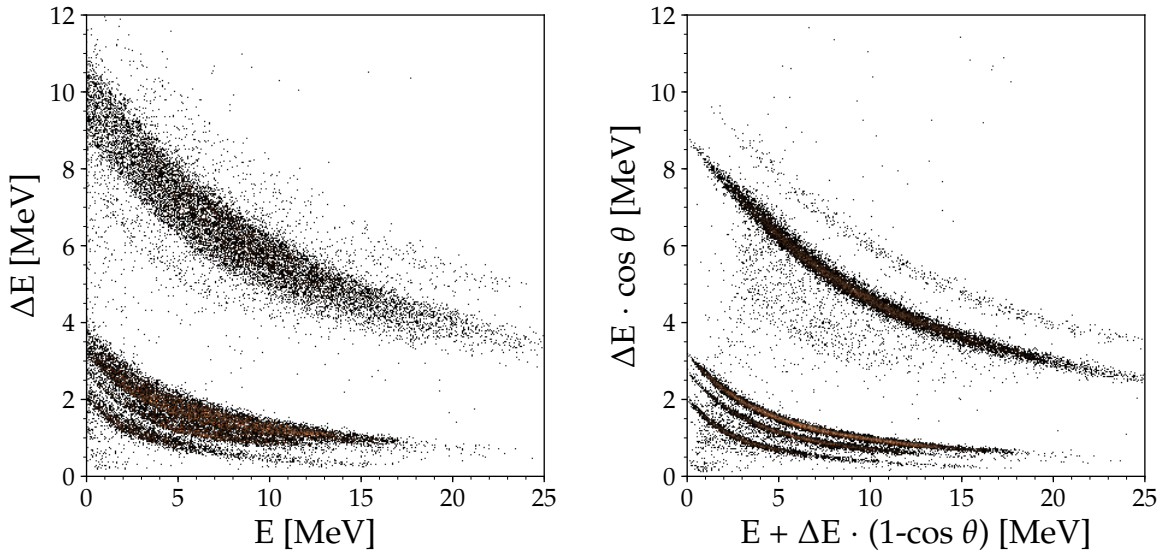

(a) (b)

Figure 3.4: $\Delta E - E$ plots without (**a**) the correction and with the correction (**b**). It is clear that we can make a much better distinction between the particles after the correction.

to the peak position. A linear function is then fitted to get the conversion between channel and energy

$$E = a \cdot \mathrm{ch} + b$$

The α-sources contains subcomponents, which are not always directly visible due to the resolution of the detector. Nonetheless, we need to take these into account too, using a sum of Gaussians for each peak.

The α-particles goes through the dead layer of the detector, before depositing it's energy in the active part of the detector. Therefore the actual measured energy is shifted down, depending on the incident angle of the particle.

For the DSSD we correct this by subtracting an average of the energy loss in each pixel from the reference α energy before performing the linear fit. This is weighted by the solid angle of the detector

$$E' = E_\alpha - \sum_{\text{pixel}} E_{\text{loss}} \frac{\Omega_{\text{pixel}}}{\Omega_{\text{strip}}} \tag{3.5}$$

For the pads we have unfortunately no spatial information, since we only have one segment. We therefore use the energy loss corresponding to α particles hitting the center of the pad.

4 Data analysis

A typical nuclear reaction experiment easily generate a large amount of data. An efficient data analysis pipeline is required to efficiently process the amounts of data and extract the interesting features. A very versatile software package has been developed at CERN to exactly this type of experiments; the ROOT package [29].

In Aarhus there has been an ongoing development of framework that builds on top of ROOT. It is designed to handle the type setups we use, which usually consists of a large number of DSSDs. Especially the geometrical representation of such detectors has been have been streamlined. This makes it very easy to calculate geometrical properties such as pixel positions in absolute coordinates, solid angles etc.

4.1 Kinematics

In the experiments we consider two particle reactions

$$A + a \rightarrow B + b,$$

where a is the target particle and is thus at rest and A is the beam particle. We will let B be the heavy recoil, which is usually the particle of interest and b be the light ejectile. We will furthermore assume that neither of the beam, target or ejectile will be in an excited state, the excitation energy E^* will always belong to B. From conservation of energy and linear momentum, we have

$$\begin{aligned} T_A &= T_b + T_B + E^* - Q \\ \bar{p}_A &= \bar{p}_B + \bar{p}_b. \end{aligned} \tag{4.1}$$

We can now calculate the momentum of B

$$\begin{aligned} \bar{p}_B &= \bar{p}_A - \bar{p}_b \\ &= \sqrt{2T_A m_A}\hat{n}_A - \sqrt{2T_b m_b}\hat{n}_b, \end{aligned} \tag{4.2}$$

where m_i is the mass, T_i is the kinetic energy and $\hat{n}_i$ is the unit vector in the direction of the particles movement, given as

$$n_i = \frac{(x_i - x_A, y_i - y_A, z_i - z_A)}{\sqrt{(x_i - x_A)^2 + (y_i - y_A)^2 + (z_i - z_A)^2}}, \tag{4.3}$$

where (x_i, y_i, z_i) is the position in space where we detected the particle and (x_A, y_A, z_A) is the beam position.

The excitation energy can now be calculated using (4.2) and (4.1)

$$E^* = T_A - T_b - \frac{\bar{p}_B^2}{2m_B} + Q. \tag{4.4}$$

4.2 Differential cross sections

Together with the excitation energy, we are interested in the differential angular cross section. From this, we can extract the transfered angular momentum of the ejectiles, and thus deduce the states that were populated in a given reaction. A differential angular cross section can be interpreted as the probability for a particle to be emitted in a given solid angle. From an experimental point of view the differential angular cross section is given as

$$\frac{\mathrm{d}\sigma}{\mathrm{d}\Omega}(\theta,\phi) = \frac{\dot{N}_b(\theta,\phi)}{I_A \cdot n_t}\frac{1}{\mathrm{d}\Omega}, \tag{4.5}$$

where $\dot{N}_b$ is the rate of the reactions, I_A is the beam intensity, n_t is the number of target particles per area and $\mathrm{d}\Omega$ is the solid angle. We can write it in terms of the total number of particles instead of rates

$$\frac{\mathrm{d}\sigma}{\mathrm{d}\Omega}(\theta,\phi) = \frac{1}{n_t}\frac{1}{N_A}\frac{N_b(\theta,\phi)}{\mathrm{d}\Omega}, \tag{4.6}$$

where the last fraction describes the number of particles in a given solid angle and N_A is the total number of beam particles.

Not all particles will, however, hit the detectors. There will be some angle dependent efficiency that we must account for

$$\left(\frac{N_b(\theta,\phi)}{\Omega}\right)_{measured} = \frac{N_b(\theta,\phi)}{\Omega}\cdot\epsilon, \tag{4.7}$$

where ϵ is 1 if we register all particles in a given solid angle and 0 if we register none.

To account for the efficiency of the detectors we can simulate N_A^{sim} reactions uniformly distributed in 4π and count the number we register in the detectors, $N_{\mathrm{det}}^{\mathrm{sim}}$. The efficiency is

$$\epsilon = \frac{N_{\mathrm{det}}^{\mathrm{sim}}(\theta,\phi)}{N_A^{\mathrm{sim}}(\theta,\phi)}\frac{1}{\mathrm{d}\Omega} \tag{4.8}$$

Combining 4.6, 4.7 and 4.8 we can write the differential cross sections as

$$\frac{\mathrm{d}\sigma}{\mathrm{d}\Omega}(\theta,\phi) = \frac{1}{n_t}\frac{N_{det}^{exp}(\theta,\phi)}{N_{det}^{sim}(\theta,\phi)}\frac{N_A^{sim}}{N_A^{exp}}. \tag{4.9}$$

The numbers $N_{det}^{exp}(\theta,\phi)$ and $N_{det}^{sim}(\theta,\phi)$ are found through particle identification, as described in section 3.3. N_A^{sim} is known from the simulation. The particle density in the target, n_t can be calculated based on known parameters. The hardest number to determine is the total number of beam particles, N_A^{epx}.

4.3 Geometry, energy and beam properties

The reconstruction of the excitation energies and angular distributions relies heavily on precise knowledge of good energy calibrations, precise detector and beam spot position, beam angle and beam energy. We therefore need to invest some effort in determining these properties as the first step in an analysis.

The usual method to energy calibrate the detectors is with an α-source with a well-known energy spectrum. This works very well, but the energy range of the α spectra usually extends up to 6 MeV - 8 MeV. This means we have to extrapolate this calibration when doing reaction experiments where the particles have much higher energies. In IS561 we had a beam energy of 6.72 MeV / A, meaning the elastic deuterons had up to approximately 30 MeV.

The energy deposited in the DSSDs is within the range of the calibration, gravitating to the lower energies, due to their thicknesses of 60 µm. This means the majority of the energy is deposited in the pad, which was calibrated in the same way. It is thus necessary to at least check that the calibration of the pads in the high energy range is viable.

One method that comes to mind is to look at the kinematic curves of an elastic channel. They are, after all, well understood by simple kinematics theory. The trouble now, is that to get a reliable kinematic curve from a detector, we must be sure about the geometry of the detector and the beam properties.

On the contrary, to determine the beam properties, as described in a later section, we can use the kinematics of detected coincidence events. To do that, of course, we need a well understood geometry and energy calibration of the detectors.

Using kinematics to solve this, we need to find the right value of some very correlated variables, and it is not feasible to optimize all of them simultaneously. We must therefore use different methods and a lot of consistency checks to make sure we the correct values out.

Hardware measurements: For the geometry part one could simply grab the closest ruler and measure the setup. However, with very flexible setups this has shown difficult to do with the precision needed to match the 2 mm precision of the DSSDs. Using 3D printed structures we can get the relative geometry of the detector with sufficient precision. This was done for the second experiment but not the first.

Uniform distributions: We can use the uniform distribution from the α source to fit the position of the detectors. This is independent of both the beam and the energy calibration and is thus very useful. As we will discuss in Section 6.2 we can get a relatively good understanding using this method. This of course requires that we know the position of the source.

Particle identification: The $\Delta E - E$ spectra should in principle not depend on any geometry, however, with the correction (3.4) we introduce an angular dependence. If we align the bands of the different particles, this servers as a useful consistency check among the detectors. This is dependent on the calibration and position of the detectors and beam position, but not the beam energy. These spectra typically contains multiple particles, which gives a few more constraints.

Coincidences Coincident fragments are very useful to check consistency between particles. The simplest check is the ϕ-angle between two particles, which should be 180°.

Including the energy of the particles we can try to reconstruct the beam based on energy and momentum conservation as described in Section 5. This will serve as a very useful cross check since it uses coincidences in all detectors. However, if the energy calibrations of the pads are not good enough, we will use the wrong energies in the calculations of energy conservation and momentum conservation. This will in turn give a wrong behavior of the coincidences.

Pad calibrations

We can now use two alternative methods to calibrate a pad at higher energies. They are both based on that we know the energy in the DSSDs and that we can calculate the expected energy loss with SRIM[30].

Calculate energy loss with SRIM This method does not depend on the beam energy. It does, however, depend on that we know the beam spot. For each particle penetrating the DSSD, we can take the energy in the DSSD and calculate what initial energy it corresponds to using SRIM. The rest of this energy should then match what was deposited in the pad.

Fit to kinematic curves Once we have isolated a clean reactions channel (the elastic scattered deuterons are typically clean), we can vary the slope and offset of the pad calibration to fit the theoretical kinematic curve. This, however, requires that we know both beam energy, beam spot and the geometry of the detectors.

4.4 Software

4.4.1 ROOT

The back bone of the data analysis is the very feature rich framework ROOT[29]. It is written in the C++ programming language. It excels in quite a number of areas, but in particular its support for histograms, which is a requirement for any nuclear data analysis, is very good.

The main data structure in ROOT is the TTree-class. It organizes the data in events, structured via so called Branches. A branch is the abstraction of some value recorded for each event, such as detector energy, strip hit, time stamp, etc. It can be thought of as a very flexible table. A branch then corresponds to a column and an event corresponds to a row.

One major advantage of the TTree is the very sophisticated Draw-command. You can open a TTree in an interactive ROOT session and make cuts directly in your data. This means you do not have to rewrite and recompile your program whenever you want to explore a new area of your data. It is thus very handy for quick analysis. At some point we need to do a more sophisticated analysis, but we keep results as TTree instead of histograms. Then the needed histograms can be generated quickly and we do not need to consider binning, ranges, etc, during the actual analysis.

4.4.2 AUSAlib

To do the more sophisticated analysis, another framework was developed on top of ROOT, here in Aarhus. Much of the core was done by Michael Munch with contributions from Oliver Kirsebom when I started. I have contributed extensively to the further development during my analysis work.

It is also written in the C++ programming language. The philosophy of AUSAlib is twofold. Firstly, it generalizes the detector properties, in particular the geometrical properties. This means we only have to implement solid angle calculations and pixel position calculations one time for a particular type of DSSD (Square, Round, etc). Secondly, it makes the analysis very modular, and it is therefore easy to perform analysis on different levels of sophistication.

To ease use, all geometry specific and energy calibrations can be loaded into the analysis code through JSON file. It consists of an array of detector entries. Each entry specifies

- **A detector file** This describes the type. Examples are SquareDSSD, RoundDSSD, Pad and more. Each type requires additional information such as physical dimensions, number of segments, deadlayers etc.
- **Position and orientation** Each detector type are uniquely positioned and rotated in space via three vectors. They are indicated for the square and round type in Figure 3.2.
- **Calibration** A file with the calibration of the particular detector.
- **Mapping** Details on the data layout in the data files corresponding to this setup.

The pipeline of a typical analysis is shown in Figure 4.1. The idea is to transform the data at each stage to a higher level of abstraction. We start with raw channel numbers and end at actual physics events. At every stage, is it possible to write a custom analysis.

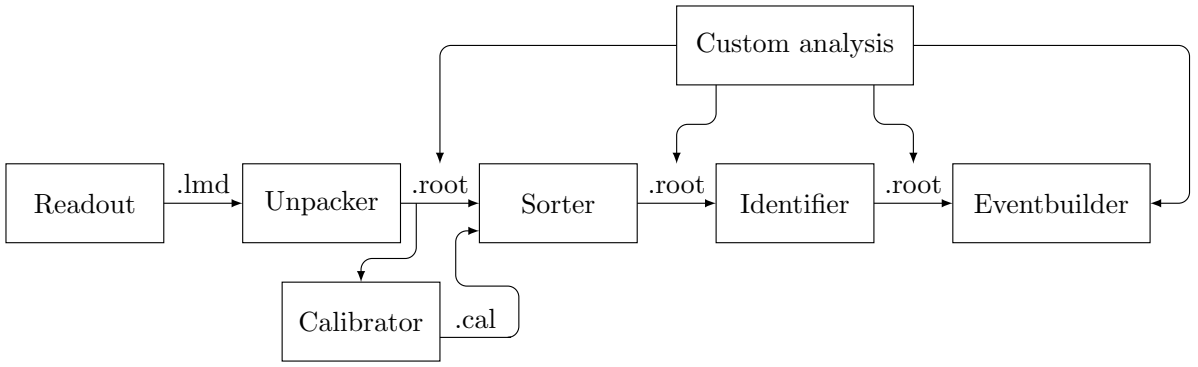

Figure 4.1: The AUSAlib pipline.

Besides the advantage that we can share code and be more productive, it is much easier to catch bugs when more people use the same piece of code. This makes the core of the analysis code very robust.

Most of my analysis takes place after the Sorting stage or after the EventBuilder stage.

Unpacking and calibration First we get the raw data from the detection read out system. It is then unpacked using *ucesb* [31], producing ROOT-files. At this stage one can write a custom made analysis, handling raw channel numbers.

An important analysis is calibration of all segments. AUSAlib provides a built in Calibration tool to ease this process, using the principles discussed in 3.4. It is, however, not limited to α-sources.

Sorting With the calibrations of each detector, we run the data through a sorting algorithm, using a built in Sorter tool. This applies the calibrations of each segment to the data. After the calibration of all the segments we perform a matching of the data to make sure our data makes sense in DSSD's. When a particle hits the detectors, it will deposit rougly the same energy in both the front and back side. This means, if we observe a single hit in the front, but nothing in the back we discard it as non-physical. Likewise, if the energy in the front side and back side are very different, we also consider it non-physical. That means we require the data from the DSSD's to be within some *matching gate*, Δ

$$|E_{\text{front}} - E_{\text{back}}| < \Delta. \tag{4.10}$$

The size of Δ depends on the resolution of the data and is therefore experiment and setup specific.

The Sorter-tool generates ROOT files and we can now write an analysis where we handle energies instead.

Identifier With the sorted data it is possible to start doing particle identification, for instance with $\Delta E - E$ cuts. Once we have identified the particles we can start doing energy loss corrections in the target and dead layers of the detectors. At the identifier stage, we move from a detector based structure to a particle based structure.

EventBuilder At the last step in the pipe line we construct the entire kinematics of each physics event. From the identified file we get the particle type, energy and hit position. The user supplied the beam properties, and using momentum and energy conservation we can reconstruct the entire event.

5 Beam diagnostics

The simplest model of the beam in reaction experiments is a point like beam hitting the target in the center. This is, however, never the case. The beam is typically broad, displaced and even angled. Some of these effect can be minimized through careful alignment and collimation of the setup.

In particular the displacement and the angle of the beam is important when reconstructing the particle energies and momenta in the analysis. If the geometrical assumptions of the beam are wrong we introduce an unnecessary bias in the analysis, leading to worse resolution and wrong angular distributions.

To deduce the beam properties of the beam, we can use coincidences since they in principle contain the full energy and momentum information. Using energy and momentum conservation we can calculate backwards to deduce the beam properties. A great advantage of this method is that we can use it directly on the reactions of scientific interest. The method is based on [32].

5.1 Theory

We can do the same calculations as we did in Section 4.1, but isolate the beam instead. If we combine energy conservation and momentum conservation requirements we get

$$T_b + T_B + E^* - Q = \frac{T_B m_B + T_b m_b + 2\sqrt{T_B m_B T_b m_b}\hat{n}_B \cdot \hat{n}_b}{m_A}. \tag{5.1}$$

Finding the solutions to (5.1) is a matter of doing a numerical minimization of the difference between the LHS and the RHS. This is done for every pair of coincident particles.

From the beam position we can calculate the angle of the beam in spherical angles

$$\tan(\theta_A) = \frac{\sqrt{p_{A,x}^2 + p_{A,y}^2}}{p_{A,z}} \qquad \text{and} \qquad \tan(\phi_A) = \frac{p_{A,y}^2}{p_{A,x}}$$

5.2 Simulations

We can test this method against simulations, and we will use the setup shown in Figure 5.1a. This setup inspired the design of the setup used in IS561. Doing a simulation of a ^{9}Li (d,d)^{9}Li reaction, the result is shown in Figure 5.1b. We can clearly see the structure of the setup featured in the data. The four "arms" corresponds to each of the surrounding detectors.

During development of this method, we realized that we have to think in terms of *reaction planes*. Each particle pair will move in a plane, spanned by the two particle momenta. All of the particle pairs would origin from the same beam spot, and the intersection of all these planes is then the reaction site. If the we had exact measurements of the particles we would see a point in Figure 5.1b, but due to the limited position and energy resolution we see an extended distribution.

Looking at single reaction planes are not possible. Instead we can make a crude approximation, and treat coincidences between one of the peripheral detectors and the center detectors as one plane. If we do that we get the distributions shown in Figure 5.1c. As we can see, the resolution on the axis that is expected to be the reactions plane is much better than the orthogonal axis.

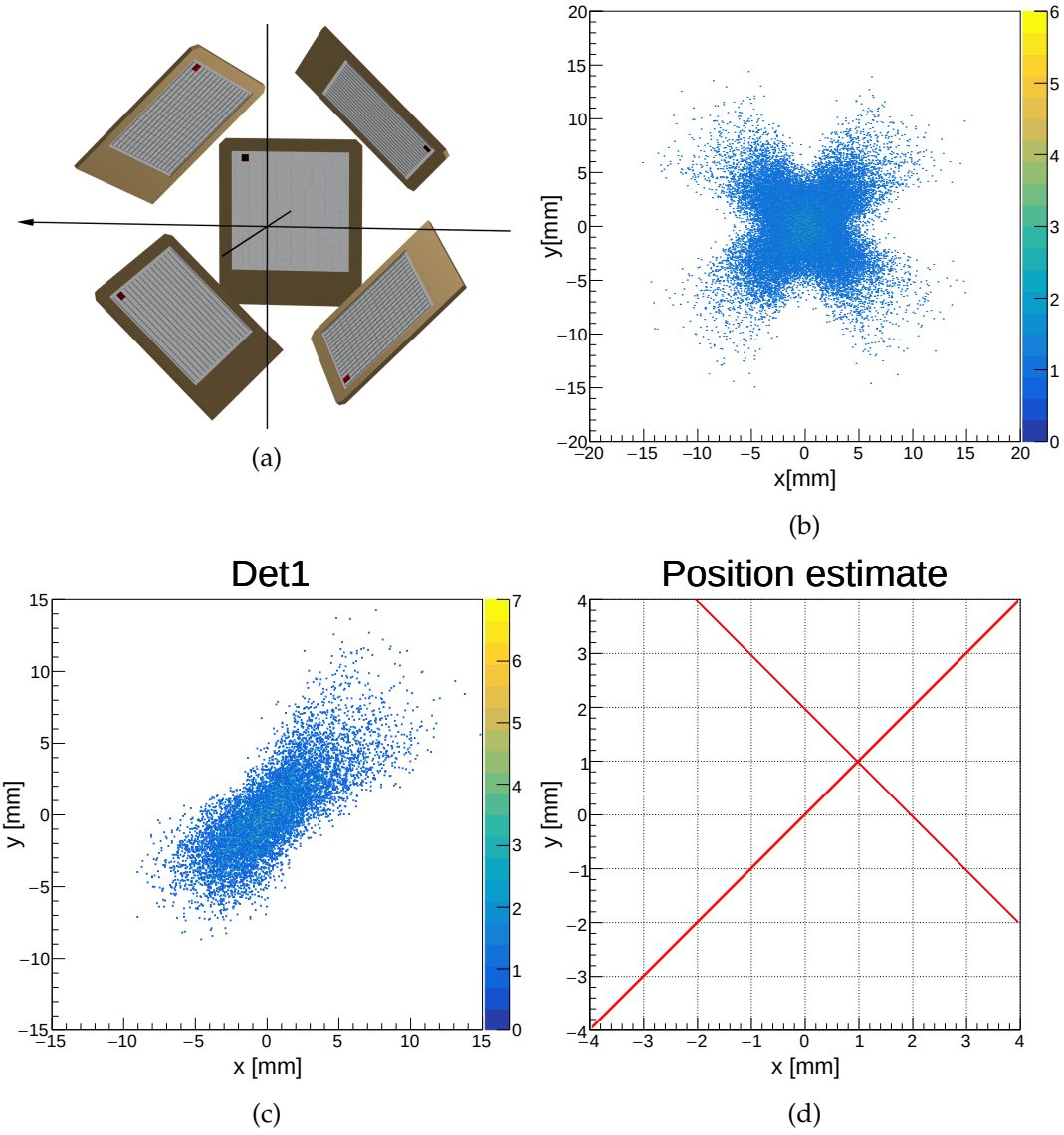

We can now fit a line, to this distribution. This line is an estimate of one reactions plane. In Figure 5.1d we have simulated a beam incident at (1 mm,1 mm), and we have made an estimate of the reaction plane for each of the pheriferical detectors. The lines cross nicely very close to (1 mm,1 mm). Notice that it seems like there is only two lines, but due to the symmetry, there are actually four, but they overlap pairwise. This also means that there is a small bias in the methods, since we are not exactly in (1 mm,1 mm).

The division of the data into these regions is done rather arbitrarily. The smaller regions, the better resolution we expect to get. Therefore, it is very much up to the specific experiment and setup to decide on the sections used. If there are plenty of statistics, one might even take only the few center strips.

The important thing is to cover several regions uniformly in ϕ. We need to get contributions from all directions to get a proper determination of the crossing point. Therefore a large ϕ-coverage is required for this method.

6 IS367

I started with analysis of an experiment carried out in May 2006. It was the continuation of an experiment carried out in 2002, but with improved detectors, targets and more statistics.

The goal was to study the unbound nucleus ^{10}Li via a one nucleon transfer reaction. It was performed at REX-ISOLDE at 2.77 MeV/A. At this energy it is possible to study the excitation spectrum of ^{10}Li up to around 1 MeV. In this range it should be possible to locate both the $1s_{1/2}$ and the $0p_{1/2}$ states and thus provide more experimental data to understand the system.

6.1 Setup

The experimental setup consisted of two silicon telescopes. A sketch of the setup is shown in Figure 6.1a. Each telescope had a 60 µm front detector of the BB7 type, i.e. 32x32 strips. The back detectors were roughly 1.5 mm.

In the center was a target ladder placed with different targets as described in Table 6.1.

Table 6.1: The different target used in IS361.

Target	Thickness	Usage
CD_2	15 µm	The main target. Used in majority of the experiment for $^9\text{Li} \rightarrow d$.
CD_2	7.5 µm	A thinner main target. It was only used for approximately one hour.
CH_2	15 µm	Background estimate of $^9\text{Li} \rightarrow p$ reaction.
^{12}C	2 mg/cm^2	Background estimate of $^9\text{Li} \rightarrow C$ reaction.
^{9}Be	1.95 mg/cm^2	Not considered in this analysis.
^{107}Ag	1.1 mg/cm^2	Yield estimate based on Coulomb scattering.

6.2 Data analysis

Energy calibration

The first step of the analysis is an energy calibration of the detectors. During the experiment several data files were recorded with two different α-sources in the target position. One source consisted of ^{244}Cm, ^{241}Am and ^{239}Pu. The other was only ^{148}Gd. Using the procedure in Section 3.4, we can calibrate each strip in the two DSSDs.

The pads were likewise calibrated using the same two α-sources. For the pad calibrations, however, the sources were placed behind the telescopes and thus hitting the pads from the back.

Particle identification

With an energy calibration and a rough geometry estimate we can use the $\Delta E - E$ method to identify the different particles. In Figure 6.1b we see all the particles that penetrated the DSSDs and entered the pad.

The three lower components are the three expected hydrogen isotopes: protons, deuterons and tritons. The upper one is the triton. It loses relatively more energy in the DSSD due to the greater mass.

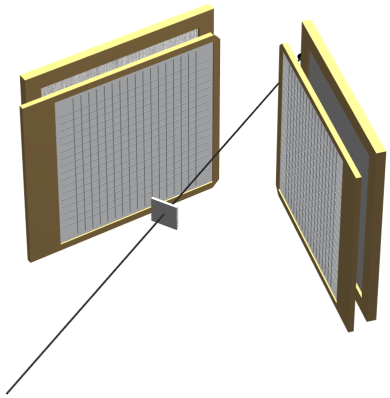

(a)

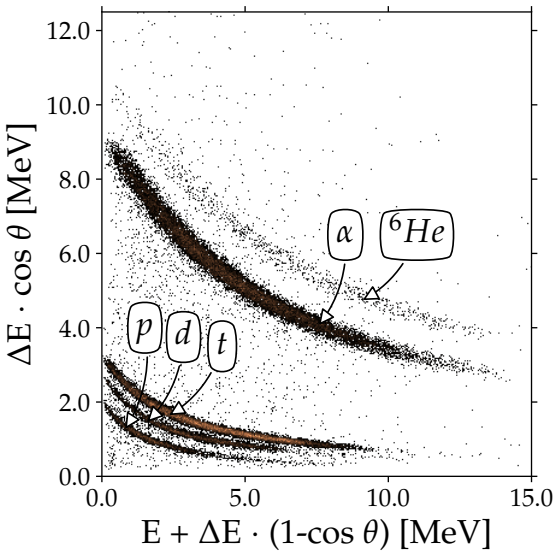

(b)

Figure 6.1: **(a):** The setup consists of two DSSDs, each backed by a pad. In the middle is the target sketched. **(b):** The $\Delta E - E$ plot clearly shows protons, deuterons, tritons, α-particles and ^{6}He

In the top of the spectrum we see a large band, corresponding to α-particles. Many α-channel are open from ^{9}Li reactions with both deuterons, protons or ^{12}C, contributing to the rather intense band. Just above we see a weak band, that corresponds to ^{6}He. These two particles have not been analyzed yet.

Geometry calibration

The telescopes were placed in the chamber and approximate measurements were made with a ruler. As discussed we need to know the precise position of the detectors, and we used the isotropic distribution of the α source to fit the positions of the detectors.

We assume the α-particles are emitted isotropic from the source. The expected number of α particles in a single pixel is proportional to the solid angle with some proportionality constant A, which depends on the total number of emitted α particles

$$N_e(i,j) = A\Omega(i,j), \tag{6.1}$$

where A is common for all detectors. This is to be compared with the measured number of particles, $n_{i,j}$. We can estimate the position of the detector relative to the source position, by fitting this to the actual number of measured particles.

This method is, however, not very sensitive to the the normal direction of the detector. The $\Delta E - E$ plot are, however, due to correction (4.7). The trouble is now, that both the position, the normal direction and the beam position determine the incident angle of the particle. Therefore I employed an iterative approach to get consistency between the two detectors:

- Use the geometry calibration method described above to get a position estimate for each detector.
- Pick a region of the α branch where the curve is flat. Calculate the mean value of the counts in this region for each DSSD and minimize

$$\min\left(\Delta E^{\text{avg}}_{\text{DSSD1}}(\theta_1) - \Delta E^{\text{avg}}_{\text{DSSD2}}(\theta_2)\right). \tag{6.2}$$

The second step only determines the the angles locally among the two detectors, but in conjunction with the global position fit it worked nicely. The results are shown in Table 6.2.

Detector	x[mm]	y[mm]	z[mm]	θ[deg]
DSSD1	-32.68	-3.24	45.97	43.5
DSSD2	-27.44	1.1	26.92	61.9

Table 6.2: The determined positions and angles of the two DSSD's with respect to the target position.

Beam properties

With a good understanding of both the geometry and the energy calibration, we can use the method, described in 5. The algorithm depends on the kinematics of the reaction. This means two thing. Firstly we have to know the beam energy. The beam energy reported from the experiment is 2.77 MeV/A. Secondly we need a rather clean spectrum, in order to be sure that we are using the right reaction in our calculations. This makes the elastic scattered deuterons a good choice. The elastic peak is nicely isolated from the first excited state.

If we use the reported beam energy from the experiment, we plug all the elastic scattered into the algorithm. Notice, with only two detectors we can not calculate a crossing point between different lines. In stead we simply used the projections of the x- and y-axis respectively, and we get an estimate of the beam position.

$$\begin{aligned} x &= 0.0\,\text{mm} \\ y &= 1.3\,\text{mm} \\ z &= 1\,\text{mm}, \end{aligned}$$

where the z-values was chosen to make the kinematic curves consistent as shown in Figure 6.2. Notice the component from the ^{9}Li (p,p)^{9}Li reaction, corresponding to background from non-deuterated plastic.

Excitation spectra

We reconstruct the excitation energies using 4.4. Before we proceed, we need to subtract the background. The background comes primarily from reactions with carbon and protons. During the experiment multiple background runs were performed, with the targets outlined in Table 6.1. The data from the background runs were analysed just like the deuterated target.

In Figure 6.3d we see the excitation spectra of the protons from the physics runs, superimposed with the background from the carbon run and the non-deuterated plastic run. We use the protons as model, due to the large elastic proton peak. The composition of the background will be the same in all channels.

The tail from -200 keV and downwards is fitted to the a sum of the two background spectra and we get the following composition

$$BG = 0.13(4) \cdot CH_x + 0.35(1) \cdot C. \tag{6.3}$$

After this subtraction, we get the excitation spectra from all the three channels, as shown in Figures 6.3a, 6.3b and 6.3c.

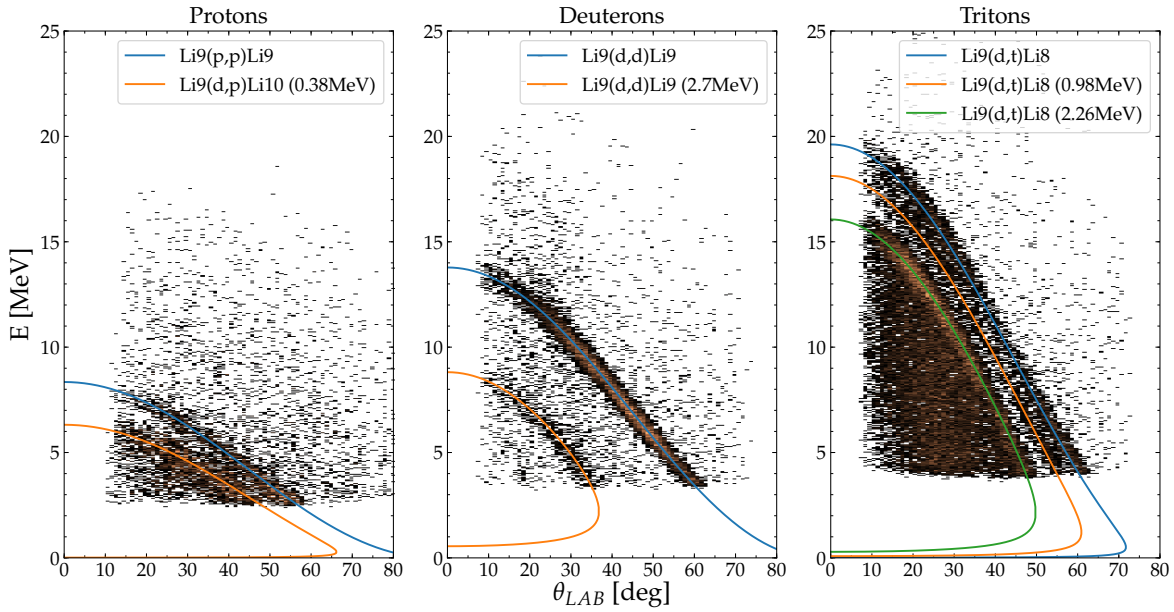

Figure 6.2: Kinematic curves for the three identified particles. We clearly see components from different excitations states. Notice the the elastic scattered protons from ^{9}Li (p,p)^{9}Li.

Differential cross sections

Following the method described in the Section 4.2, we can evaluate the different regions of interest in the excitation spectra, i.e. the different peaks.

Since I have not yet had the time to evaluate N_A^{sim} from (4.5), I will omit the constant

$$\frac{1}{n_t}\frac{N_A^{sim}}{N_A^{exp}}, \tag{6.4}$$

however, this can be estimated by Rutherford scattering on the Ag targets that was taken during the experiment.

The simulations were done using simX, a simulation program written in Aarhus [33]. For each region of interest, I simulated a uniform distribution (in CM) and recorded the detected particles. The simulated reactions were chosen to match the region, such that the recoil would have the correct excitation energy and width. The widths are based on Gaussian estimates of the excitation spectra, shown in Figure 6.3.

6.3 Results and discussion

I have not yet had the time to do calculations to compare the angular distributions. We will thus discuss some qualitative features, and compare to an earlier similar experiment where the beam energy was 2.36 MeV/A. Notice that we go to lower θ in IS367.

To compare the features of the spectra of the two experiments, we need to account for the difference in beam energy, and we can make a rough estimate. The cross section depends only on the transferred momentum, $\bar{p}_t$ through the combination $k\sin(\theta/2)$[34], where k is the momentum of the incomming particle, giving us

$$k_1 \sin\left(\frac{\theta_1}{2}\right) = k_2 \sin\left(\frac{\theta_2}{2}\right) \Rightarrow \theta_1 = 2\sin^{-1}\left(\frac{k_1}{k_2}\sin\frac{\theta_2}{2}\right). \tag{6.5}$$

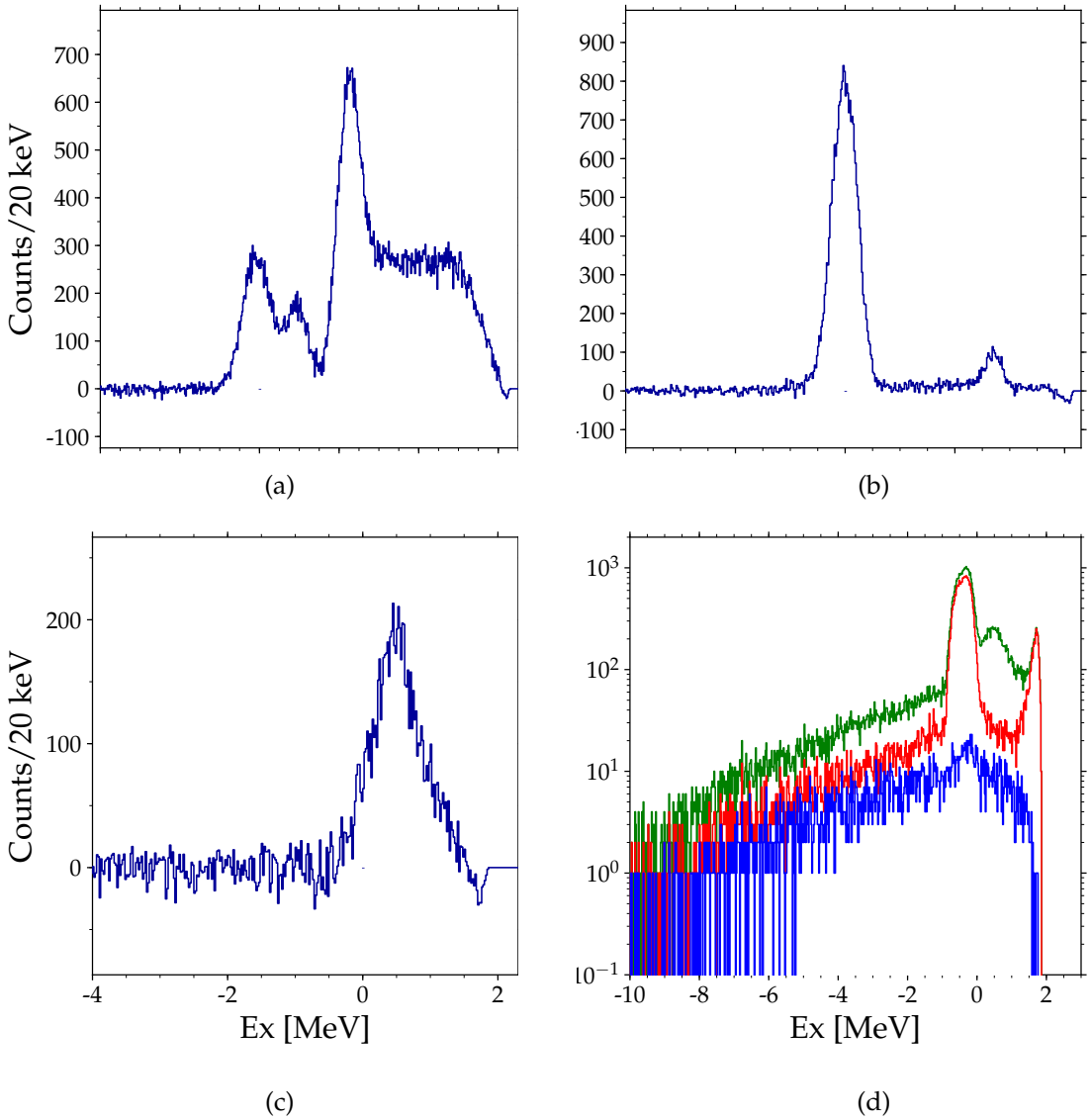

Figure 6.3: Excitation spectra for the three recoils ^{8}Li (**a**), ^{9}Li (**b**) and ^{10}Li (**c**). Background for ^{10}Li is shown in (**d**). The green is CD_x, the red is CH_x and the blue is C.

Since $k \approx \sqrt{E}$ we get $\frac{k_1}{k_2} = \sqrt{\frac{2.77\,\text{MeV/A}}{2.36\,\text{MeV/A}}} \approx 1.10$. This is the angle with respect to the beam, and since we report everything i CM, we will make the correction

$$\theta_{OLD} = 180 - 2\sin^{-1}\left(1.1 \cdot \sin\left(\frac{180 - \theta_{NEW}}{2}\right)\right).$$

We subtract 180 because we are in reverse kinematics, and therefore report angles with respect to the beam. We must also remember, that this is only valid for elastic reactions, so it only serves as an estimate.

^{8}Li Starting from the smallest nucleus, the ^{8}Li excitation spectrum is feature rich, see Figure 6.3a. We see the ground state and two peaks, corresponding to the two first excited states 0.98 MeV and 2.26 MeV.

One feature that we do not see is the discussed 0^+ state. From this preliminary analysis we can not pinpoint such a state in the excitation spectrum. The ground state and the first excited state seems consistent with the cross sections described in [19].

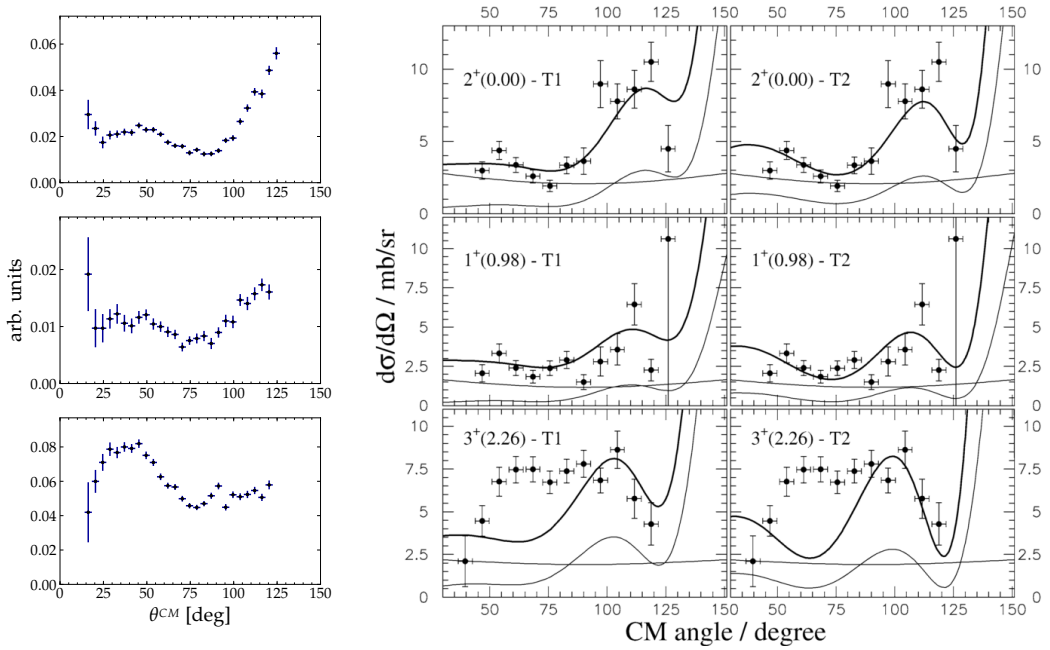

Figure 6.4: Angular distributions for ^{8}Li and the reported cross sections from [19].

In Figure 6.4 we see the angular distributions on the left and the cross sections reported in [19] on the right.

The ground state have a large increase starting around $\theta = 100$. If we make the correction, this corresponds to approximately 90°, which is consistent with [19]. We do, however, see more structure at the small CM angles, and we can make a better constrain on the optical model parameters.

If we continue to the first excited state, we see the same qualitative features, and in particular in the second excited state we have much more structure at the smaller angles.

^{9}Li In the ^{9}Li channel we see two peaks corresponding to the elastic channel and the first excited at 2.7 MeV, see Figure 6.3b. Besides that, the spectrum is clean. From the clean elastic peak, we can get an idea of the resolution of the setup. Fitting a Gaussian we get FWHM value of 551(4) keV. This can be compared with a simulated point beam which gives 440.2(6) keV. The beam must therefore have had a significant energy and spatial distribution, as expected.

If we do the same correction as before and compare with [35], see Figure 6.5, it the structure looks very similar. Keep in mind that [35] have normalized the cross sections to the Rutherford cross section. The bump at 95° in the lower panel should move to 83° which we see in the upper panel. This also means, that the optical potential parameters is more or less identical to the experiment at lower energy. Beside the kinematic difference due to another beam energy, the structure are more or less identical.

We do, however, have better information at the smaller angles, making the second optical fit in the upper panel seem more plausible. The first excited state does not show much structure.

^{10}Li In the ^{10}Li spectrum we see a single peak around the 0.5 MeV, see Figure 6.3c. Both the s-wave and p-wave is expected to be in this region. Especially the s-state is expected to be so broad that we must expect them to overlap significantly. We can, however, see that the peak is asymmetric. This may indicate of some structure in the peak. The angular distributions does, however not show much structure, see Figure 6.6. This is similar to data from [15]. Note, that the cross sections in [15] are in normal kinematics, and the angular axis is thus reversed compared to our data.

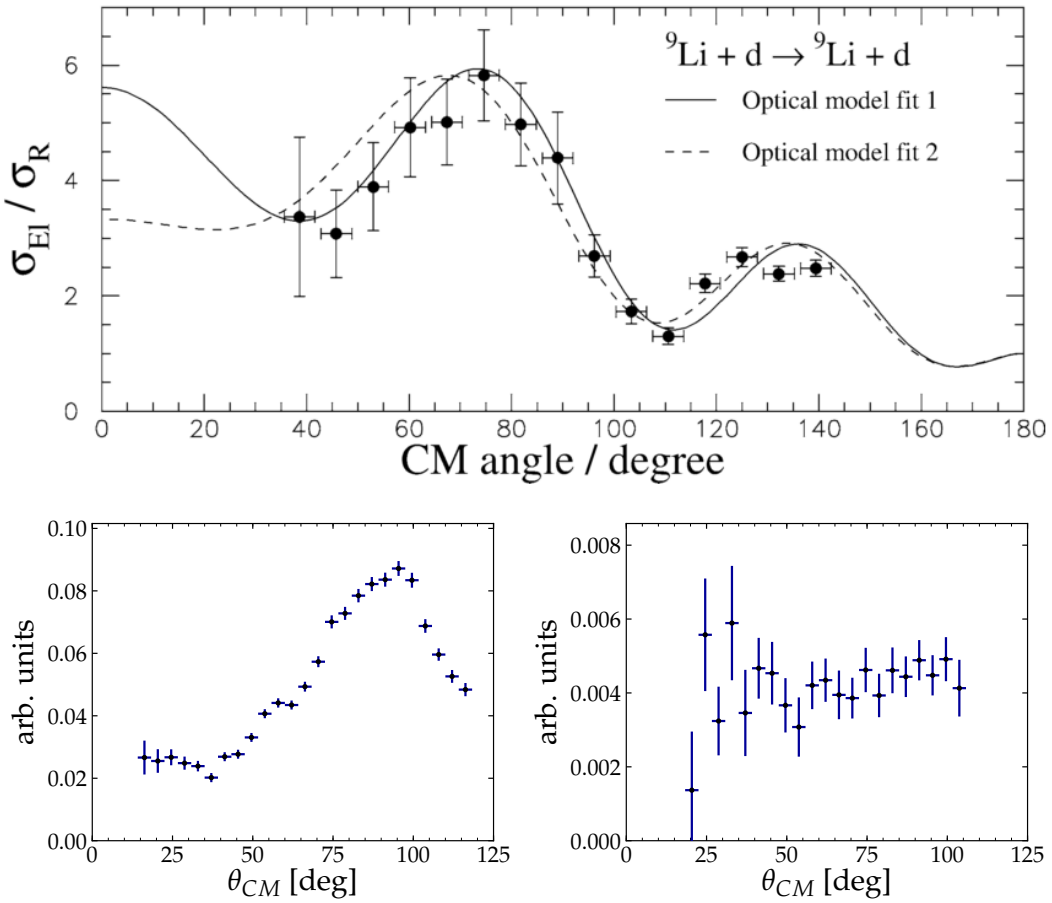

Figure 6.5: Angular distributions for ^{9}Li and the reported cross sections from [35]. The lower left is the ground state and the lower right is the first excited state. Notice that [35] have normalized to Rutherford cross sections.

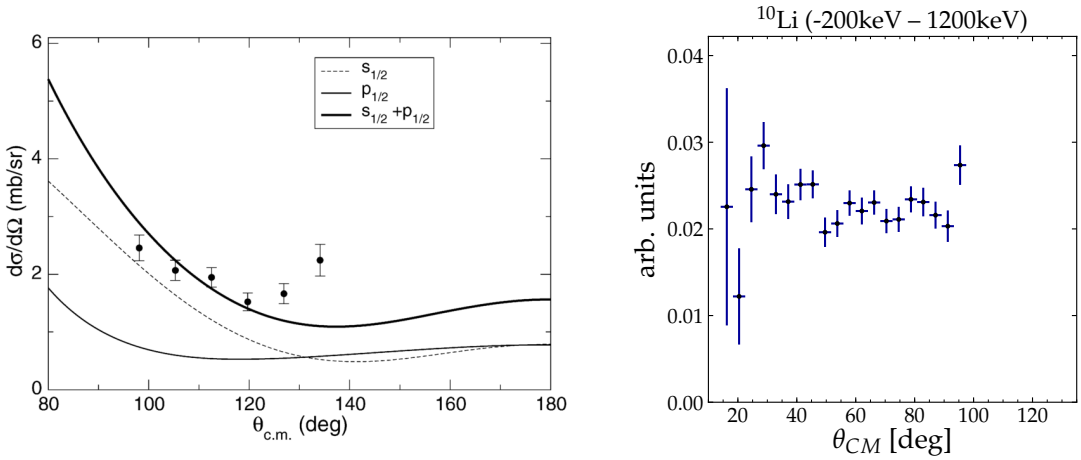

Figure 6.6: **Left:** Differential angular cross section for ^{10}Li from [15]. **Right:** The angular distributions for ^{10}Li from this experiment.

7 IS561

The first part of the experimental program was performed during the fall of 2016. The second part will be performed during the fall of 2017. During the beam time we had some problems which will propagate to the data analysis. I will briefly discuss these and present some preliminary results.

7.1 Setup

The setup is shown in Figure 7.1a. It consists of five telescopes placed in a pentagon structure with a S3 in the end of the "barrel" (1). The front detectors in the telescopes are all 60 µm W1's backed by 1000 µm pads. This setup will stop light fragments in the telescopes for particle identification. The S3 was also 1000 µm.

The idea behind the S3 was not necessarily to stop the light particles, but to stop the heavy fragments. This enables to use the technique discussed in Section 5 to do coincidence analysis. Likewise, can we use the hit pattern of all the particles on the very symmetric S3 to get a good understanding of the beam, even if the light particles punches through. The light particles can, however, be reconstructed with SRIM.

In the middle we have placed a target wheel (2). It consists of the different targets used for the experiment, as outlined in Table 7.1. The wheel can be remote controlled from the outside, such that we do not need to repump the chamber when we want to change target.

Table 7.1: The different targets used in IS561.

Target	Thickness	Usage
CD_2	8 µm	The main target. Used in majority of the experiment for $^9\text{Li} \rightarrow d$.
CH_2	6 µm	Background estimate of $^9\text{Li} \rightarrow p$ reaction.
^{12}C	2 mg/cm^2	Background estimate of $^9\text{Li} \rightarrow C$ reaction.
^{197}Ag	0.1 µm	Yield estimate based on Coulomb scattering. Backed by 3.5 µm Mylar.

In the backward directions we have another telescope (3), with a BB7 as a front detector. In Figure 7.1b we see the kinematic curves of the two reactions in question for the IS561 campaign. We can see that only the protons reach the backward laboratory angles. Hence, a detector in the backward directions will catch a very clean spectrum, corresponding to the "primary" channel of each experiment, that is either ^{10}Li or ^{11}Li.

7.2 Data analysis

Detector mapping

The connectors for the chamber were newly designed for this experiment. The mapping between the input and output, was therefore not entirely settled when we started and ended the experiment. I have therefore spend some time, figuring out these mappings. I have used α-distributions from the calibrations and coincidences from the reactions to get a reliable mapping between detector segment and ADC channel.

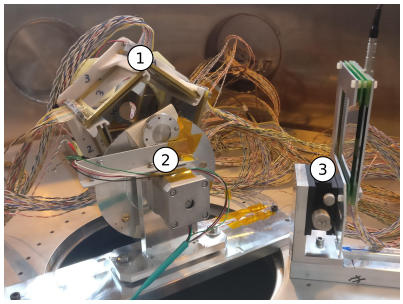

(a)

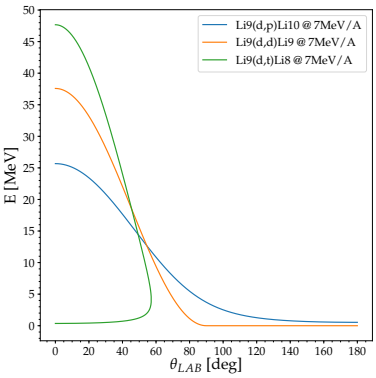

(b)

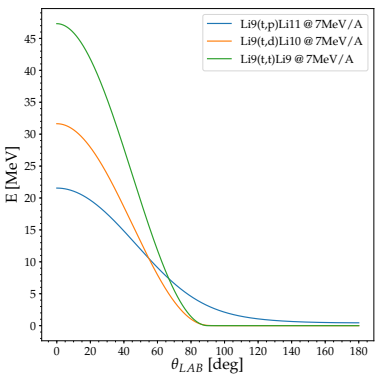

(c)

Detector geometry

The detectors were mounted on a 3D printed structure, so the relative position and spatial orientation is known to good precision. We thus only need to find out where the target was placed relative to the pentagon structure, which in the analysis coincides with the position of the beam.

Beam properties

During the run we experienced difficulties with the beam alignment. The beam was steered during the run, in order to optimize the position. This means, however, that we have two periods with slightly different beam positions. In Figure 7.2a we we see that we have implanted the beam directly in the S3 detector. In Figure 7.2b we see the hit pattern after adjusting the beam, and in Figure 7.2c we see the hit pattern after the final optimization.

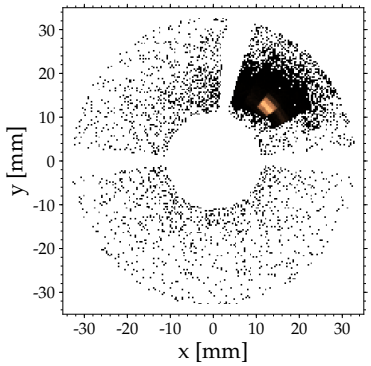

(a)

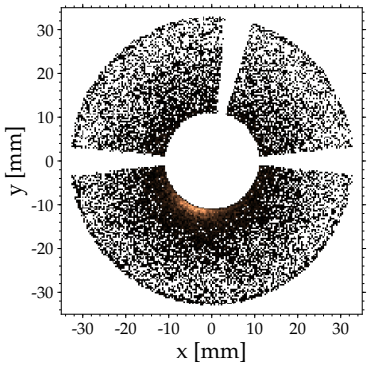

(b)

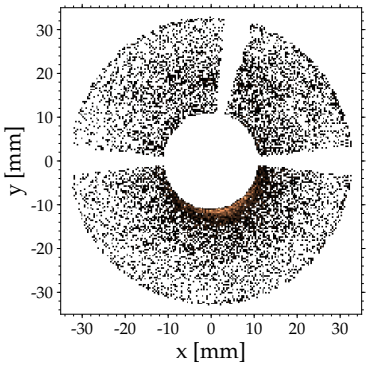

(c)

Figure 7.2: Hit patterns in the S3 from three different time periods during the experiment. **Left:** In the beginning we implanted the beam directly into the S3. **Middle and Right:** In the first part of the run our aim was better, but still shifted downwards. In the second part we shifted it slightly more to positive x-values.

It is evident that we need to determine two different beam properties. Unfortunately, the statistics is simply not good enough too perform the analysis described in Section 5. Instead we need to use the heuristics outlined in Section 4.3. This work is not done yet.

A preliminary analysis of the beam position in the first configuration gives

$$x = -2.1(5)\,\text{mm}$$
$$x = -6.1(4)\,\text{mm},$$

by fitting the angle between coincidences to π. However, this requires more consistency checks and comparisons with simulations.

During the run, the operators told us that the settings for the beam seemed to be pointing significantly downwards. This angle must also be included in the further analysis.

Pad calibrations

Due to the much higher energies the α-calibrations of the pads seems to deviate at high energies. This is expected, but must be accounted for. It was clear from the kinematic curves that the discrepancy between the measured particles and the expected kinematic curves could not only be due to geometry. I have made a preliminary calibration of the pads, by fitting the kinematic curves, but since the beam properties has not been established yet they should be revised. As a consistency check the pad energies should be compared to SRIM calculations, as described in Section 4.3, to be sure that the beam position is correct.

Preliminary physics

In Figure 7.3 we see $\Delta E - E$ plots for two telescopes in the forward direction (**(a)** and **(b)**), and the telescope in the backward angles (**(c)**). We see both protons, deuterons, tritons and αs.

Notice that we see punch through of the protons in **(a)**. Two of the telescopes were backed with a 1 mm pad whereas the three others were backed with a 1.5 mm, which means we do not stop all the protons. This is important for the next experiment, since we will go to higher energies, and thus need thicker pads.

A kinematic plot for the deuterons are shown in Figure 7.3d. We see that the amount of statistics is not impressive. However, the elastic component is clearly there. This right beam position, and pad calibrations are not determined yet, so it is a bit messy. Neither the protons or the tritons show any recognizable structures, possibly for the same reasons, and are thus not included here.

The next step is to determine these and then repeat the excitation spectra and angular distributions analysis as done for IS367. The telescope in the backwards directions not been properly analysed yet, and this is also another important task for the near furture.

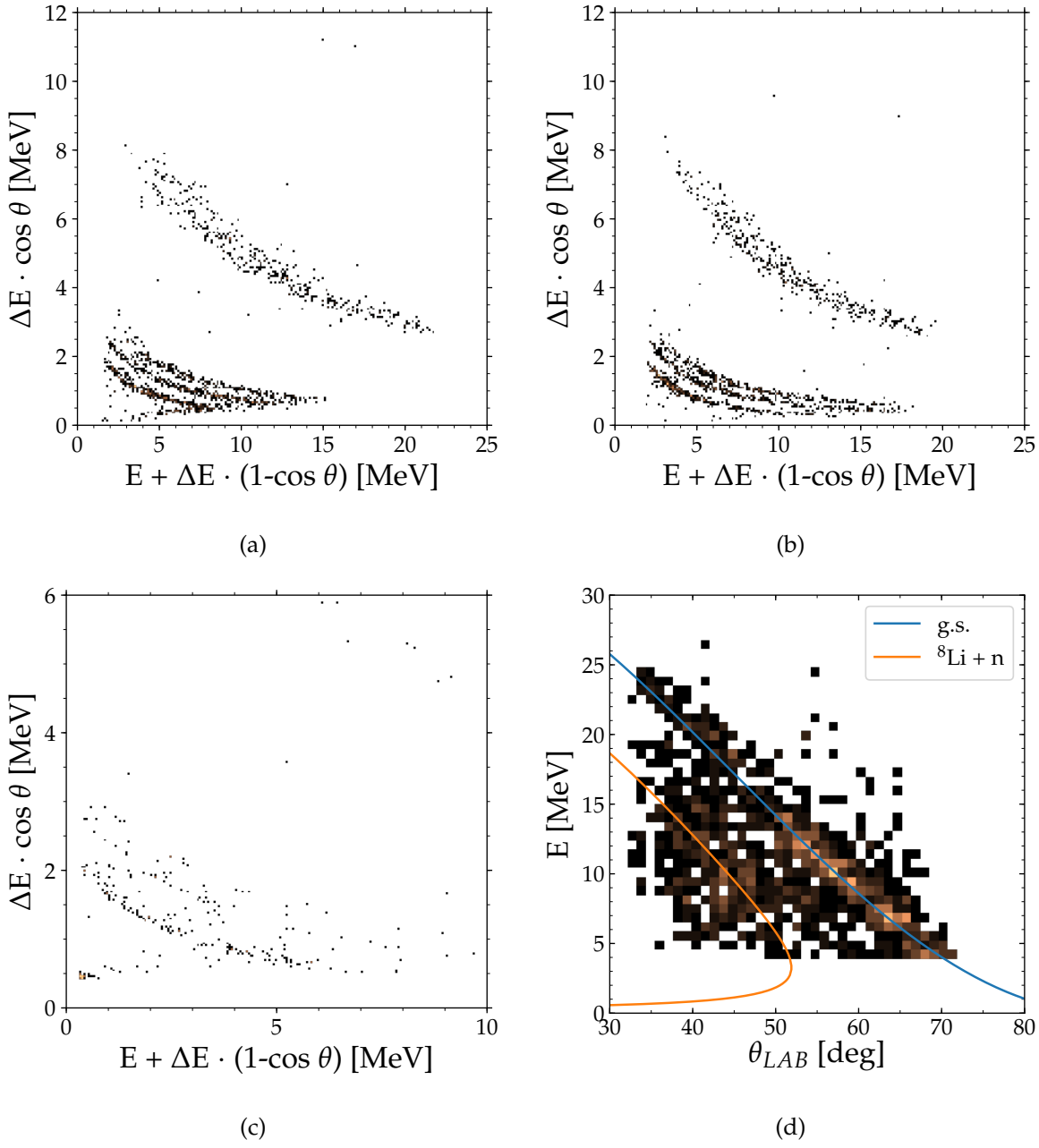

Figure 7.3: $\Delta E - E$ plots for two of the telescopes in the forward direction, (**a**) and (**b**), and the telescope in the backward direction (**c**). We clearly see the three hydrogen isotopes in the forward direction as well as α. Notice we see punch through in (**a**). In the backward telescope we have one or two components. In (**d**) we see the kinematic curves for the deuterons.

8 Outlook

The analysis of the data from IS367 is almost finished. The final step is an absolute normalization of the angular distributions to turn them into proper differential cross sections. To do this we need to know the beam intensity. During the experiment, however, several runs with a silver taget was taken. The elastic reactions are below the Coulomb barrier, and we can use these runs to determine the beam intensity from the Rutherford distribution.

The analysis of the data from IS561 is still in an early stage, but progressing nicely. I am currently working on understanding the beam properties and pad calibrations and the rest of the analysis will be very analogous to that of IS367. Alongside the physics results it has also provided useful feedback on the detection system and setup, which are currently being used to optimize the setup for the second part of IS561.

The second part is scheduled for this fall, so alongside the continued analysis of the two older data sets, I plan to stay at CERN for about two months to take part in the setup and execution of the experiment. I also spent time preparing for the first time, as well as taking part of the actual experiment, so I am already familiar with both the electronics, software and detectors. However, by staying for two full months I can be much more involved in the preparations of the DAQ and setup as well as the actual experiment. Furthermore, I will be able to learn from other experiments that will be carried out at ISOLDE in those two months.

The analysis of these three data sets will be the primary goal of my remaining Ph.D. I do, however, hope to visit an expert in theoretical calculations of these types of reactions during the fall of 2018. A possible candidate is Prof. Antonio M. Moro, from the University Of Sevilla. This would be great way to learn different theoretical techniques and frameworks to apply the results I obtain form the three experiments.

Bibliography

[1] E. Rutherford. 495 (1911), pp. 1–24.

[2] A. S. Jensen et al. *Reviews of Modern Physics* 76 (2004), pp. 215–261. DOI: 10.1103/RevModPhys.76.215.

[3] I. Tanihata et al. *Physical Review Letters* 55 (1985), pp. 2676–2679. DOI: 10.1103/PhysRevLett.55.2676.

[4] J. H. Kelley et al. *Nuclear Physics A* 880 (2012), pp. 88–195. DOI: http://dx.doi.org/10.1016/j.nuclphysa.2004.09.059.

[5] I. Tanihata. *Journal of Physics G: Nuclear and Particle Physics* 22 (1999), pp. 157–198. DOI: 10.1088/0954-3899/22/2/004.

[6] I. Tanihata, H. Savajols, and R. Kanungo. *Progress in Particle and Nuclear Physics* 68 (2013), pp. 215–313. DOI: 10.1016/j.ppnp.2012.07.001.

[7] B. R. Martin. *Nuclear and Particle Physics - An introduction*. Second edi. WILEY, 2009.

[8] J. K. Smith et al. *Nuclear Physics A* 955 (2016), pp. 27–40. DOI: 10.1016/j.nuclphysa.2016.05.023.

[9] T. Kobayashi. *Nuclear Physics A* 538 (1992), pp. 343–352. DOI: 10.1016/0375-9474(92)90784-H.

[10] K. Ieki et al. *Physical Review Letters* 70 (1993), pp. 730–733. DOI: 10.1103/PhysRevLett.70.730.

[11] S. Shimoura et al. *Physics Letters B* 348 (1995), pp. 29–34. DOI: 10.1016/0370-2693(95)00131-4.

[12] D. R. Tilley et al. *Nuclear Physics A* 745 (2004), pp. 155–362. DOI: 10.1016/j.nuclphysa.2004.09.059.

[13] I. J. Thompson and M. Zhukov. 49 (1994), pp. 1904–1907.

[14] P. Descouvemont. *Nuclear Physics A* 626 (1997), pp. 647–668. DOI: 10.1016/S0375-9474(97)00504-6.

[15] H. B. Jeppesen et al. 642 (2006), pp. 449–454. DOI: 10.1016/j.physletb.2006.09.060.

[16] M. Cavallaro et al. *Physical Review Letters* 118 (2017), pp. 1–5. DOI: 10.1103/PhysRevLett.118.012701.

[17] S. Cohen and D. Kurath. *Nuclear Physics* 73 (1965), pp. 1–24. DOI: 10.1016/0029-5582(65)90148-3.

[18] S. Cohen and D. Kurath. *Nuclear Physics A* 101 (1967), pp. 1–16. DOI: 10.1016/0375-9474(67)90285-0.

[19] H. B. Jeppesen et al. *Physics Letters, Section B: Nuclear, Elementary Particle and High-Energy Physics* 635 (2006), pp. 17–22. DOI: 10.1016/j.physletb.2006.02.034.

[20] S. C. Pieper and R. B. Wiringa. *Annual Review of Nuclear and Particle Science* (2001), pp. 53–90.

[21] P. Navrátil et al. *Journal of Physics G: Nuclear and Particle Physics* 36 (2009), p. 83101.

[22] W. N. Catford. *The Euroschool on Exotic Beams, Vol. IV*. 2014, pp. 67–120.

[23] R. Kanungo et al. *Physical Review Letters* 114 (2015), pp. 1–5.
DOI: 10.1103/PhysRevLett.114.192502.

[24] H. Simon et al. *Nuclear Physics A* 791 (2007), pp. 267–302.
DOI: 10.1016/j.nuclphysa.2007.04.021.

[25] A. A. Korsheninnikov et al. *Physical Review Letters* 78 (1997), pp. 2317–2320.
DOI: 10.1103/PhysRevLett.78.2317.

[26] S. Karataglidis et al. *Physical Review Letters* 79 (1997), pp. 1447–1450.

[27] R. Crespo, I. J. Thompson, and A. A. Korsheninnikov. *Physical Review C* 66 (2002), p. 021002.
DOI: 10.1103/PhysRevC.66.021002.

[28] *ISOLDE*.
URL: http://isolde.web.cern.ch/.

[29] R. Brun et al. *ROOT*.
URL: https://root.cern/ (visited on 07/04/2017).

[30] J. F. Ziegler. *SRIM*.
URL: http://www.srim.org/.

[31] H. T. Johansson. *The ucesb unpacker generator*.
URL: http://fy.chalmers.se/%7B~%7Df96hajo/ucesb/ucesb%7B%5C_%7Ddoc.pdf.

[32] J. G. Johansen et al. *Nuclear Instruments and Methods in Physics Research A* 714 (2013), pp. 176–187.
DOI: 10.1016/j.nima.2013.02.046.

[33] *Private communication with M. Munch and O. Kirsebom*. (Visited on 07/04/2017).

[34] P. E. Hodgson, E. Gadioli, and E. Gadioli Erba. *Introductory Nuclear Physics*. Oxford University Press, 2003. ISBN: 0-19-851897-8.

[35] H. B. Jeppesen et al. 748 (2005), pp. 374–392.
DOI: 10.1016/j.nuclphysa.2004.11.013.